

Computed optical interferometric tomography for high-speed volumetric cellular imaging

Yuan-Zhi Liu,^{1,2} Nathan D. Shemonski,^{1,2} Steven G. Adie,³ Adeel Ahmad,^{1,2}
Andrew J. Bower,^{1,2} P. Scott Carney,^{1,2} and Stephen A. Boppart^{1,2,4,*}

¹Beckman Institute for Advanced Science and Technology, University of Illinois at Urbana-Champaign,
405 North Mathews Avenue, Urbana, Illinois 61801, USA

²Department of Electrical and Computer Engineering, University of Illinois at Urbana-Champaign,
1406 West Green Street, Urbana, Illinois 61801, USA

³Department of Biomedical Engineering, Cornell University, 101 Weill Hall, Ithaca, New York 14853, USA

⁴Departments of Bioengineering, University of Illinois at Urbana-Champaign, 1304 West Springfield Avenue,
Urbana, Illinois 61801, USA

*boppart@illinois.edu

Abstract: Three-dimensional high-resolution imaging methods are important for cellular-level research. Optical coherence microscopy (OCM) is a low-coherence-based interferometry technology for cellular imaging with both high axial and lateral resolution. Using a high-numerical-aperture objective, OCM normally has a shallow depth of field and requires scanning the focus through the entire region of interest to perform volumetric imaging. With a higher-numerical-aperture objective, the image quality of OCM is affected by and more sensitive to aberrations. Interferometric synthetic aperture microscopy (ISAM) and computational adaptive optics (CAO) are computed imaging techniques that overcome the depth-of-field limitation and the effect of optical aberrations in optical coherence tomography (OCT), respectively. In this work we combine OCM with ISAM and CAO to achieve high-speed volumetric cellular imaging. Experimental imaging results of *ex vivo* human breast tissue, *ex vivo* mouse brain tissue, *in vitro* fibroblast cells in 3D scaffolds, and *in vivo* human skin demonstrate the significant potential of this technique for high-speed volumetric cellular imaging.

©2014 Optical Society of America

OCIS codes: (170.4500) Optical coherence tomography; (090.1000) Aberration compensation; (180.3170) Interference microscopy; (170.6900) Three-dimensional microscopy; (110.1758) Computational imaging; (100.3200) Inverse scattering.

References and links

1. M. Rajadhyaksha, M. Grossman, D. Esterowitz, R. H. Webb, and R. R. Anderson, "In vivo confocal scanning laser microscopy of human skin: melanin provides strong contrast," *J. Invest. Dermatol.* **104**(6), 946–952 (1995).
2. Y. Zhao, B. W. Graf, E. J. Chaney, Z. Mahmassani, E. Antoniadou, R. Devolder, H. Kong, M. D. Boppart, and S. A. Boppart, "Integrated multimodal optical microscopy for structural and functional imaging of engineered and natural skin," *J. Biophotonics* **5**(5-6), 437–448 (2012).
3. D. Huang, E. A. Swanson, C. P. Lin, J. S. Schuman, W. G. Stinson, W. Chang, M. R. Hee, T. Flotte, K. Gregory, C. A. Puliavito, and J. G. Fujimoto, "Optical coherence tomography," *Science* **254**(5035), 1178–1181 (1991).
4. F. E. Robles, C. Wilson, G. Grant, and A. Wax, "Molecular imaging true-colour spectroscopic optical coherence tomography," *Nat. Photonics* **5**(12), 744–747 (2011).
5. J. A. Izatt, M. R. Hee, G. M. Owen, E. A. Swanson, and J. G. Fujimoto, "Optical coherence microscopy in scattering media," *Opt. Lett.* **19**(8), 590–592 (1994).
6. S. A. Boppart, B. E. Bouma, C. Pitris, J. F. Southern, M. E. Brezinski, and J. G. Fujimoto, "In vivo cellular optical coherence tomography imaging," *Nat. Med.* **4**(7), 861–865 (1998).
7. V. J. Srinivasan, H. Radhakrishnan, J. Y. Jiang, S. Barry, and A. E. Cable, "Optical coherence microscopy for deep tissue imaging of the cerebral cortex with intrinsic contrast," *Opt. Express* **20**(3), 2220–2239 (2012).
8. J. A. Izatt, M. D. Kulkarni, K. Kobayashi, and M. V. Sivak, "Optical coherence tomography and microscopy in gastrointestinal tissues," *IEEE J. Sel. Top. Quantum Electron.* **2**(4), 1017–1028 (1996).

9. R. Huber, M. Wojtkowski, J. G. Fujimoto, J. Y. Jiang, and A. E. Cable, "Three-dimensional and C-mode OCT imaging with a compact, frequency swept laser source at 1300 nm," *Opt. Express* **13**(26), 10523–10538 (2005).
10. M. Akiba and K. P. Chan, "*In vivo* video-rate cellular-level full-field optical coherence tomography," *J. Biomed. Opt.* **12**(6), 064024 (2007).
11. A. D. Aguirre, J. Sawinski, S.-W. Huang, C. Zhou, W. Denk, and J. G. Fujimoto, "High speed optical coherence microscopy with autofocus adjustment and a miniaturized endoscopic imaging probe," *Opt. Express* **18**(5), 4222–4239 (2010).
12. J. P. Rolland, P. Meemon, S. Murali, K. P. Thompson, and K. S. Lee, "Gabor-based fusion technique for optical coherence microscopy," *Opt. Express* **18**(4), 3632–3642 (2010).
13. B. A. Standish, K. K. C. Lee, A. Mariampillai, N. R. Munce, M. K. K. Leung, V. X. D. Yang, and I. A. Vitkin, "*In vivo* endoscopic multi-beam optical coherence tomography," *Phys. Med. Biol.* **55**(3), 615–622 (2010).
14. Z. Ding, H. Ren, Y. Zhao, J. S. Nelson, and Z. Chen, "High-resolution optical coherence tomography over a large depth range with an axicon lens," *Opt. Lett.* **27**(4), 243–245 (2002).
15. R. A. Leitgeb, M. Villiger, A. H. Bachmann, L. Steinmann, and T. Lasser, "Extended focus depth for Fourier domain optical coherence microscopy," *Opt. Lett.* **31**(16), 2450–2452 (2006).
16. L. Liu, C. Liu, W. C. Howe, C. J. R. Sheppard, and N. Chen, "Binary-phase spatial filter for real-time swept-source optical coherence microscopy," *Opt. Lett.* **32**(16), 2375–2377 (2007).
17. D. Hillmann, C. Lührs, T. Bonin, P. Koch, and G. Hüttmann, "Holoscopy--holographic optical coherence tomography," *Opt. Lett.* **36**(13), 2390–2392 (2011).
18. J. Mo, M. de Groot, and J. F. de Boer, "Focus-extension by depth-encoded synthetic aperture in optical coherence tomography," *Opt. Express* **21**(8), 10048–10061 (2013).
19. Y. Yasuno, J.-I. Sugisaka, Y. Sando, Y. Nakamura, S. Makita, M. Itoh, and T. Yatagai, "Non-iterative numerical method for laterally superresolving Fourier domain optical coherence tomography," *Opt. Express* **14**(3), 1006–1020 (2006).
20. L. Yu, B. Rao, J. Zhang, J. Su, Q. Wang, S. Guo, and Z. Chen, "Improved lateral resolution in optical coherence tomography by digital focusing using two-dimensional numerical diffraction method," *Opt. Express* **15**(12), 7634–7641 (2007).
21. A. Kumar, W. Drexler, and R. A. Leitgeb, "Numerical focusing methods for full field OCT: a comparison based on a common signal model," *Opt. Express* **22**(13), 16061–16078 (2014).
22. T. S. Ralston, D. L. Marks, P. S. Carney, and S. A. Boppart, "Interferometric synthetic aperture microscopy," *Nat. Phys.* **3**(2), 129–134 (2007).
23. T. S. Ralston, S. G. Adie, D. L. Marks, S. A. Boppart, and P. S. Carney, "Cross-validation of interferometric synthetic aperture microscopy and optical coherence tomography," *Opt. Lett.* **35**(10), 1683–1685 (2010).
24. B. J. Davis, S. C. Schlachter, D. L. Marks, T. S. Ralston, S. A. Boppart, and P. S. Carney, "Nonparaxial vector-field modeling of optical coherence tomography and interferometric synthetic aperture microscopy," *J. Opt. Soc. Am. A* **24**(9), 2527–2542 (2007).
25. D. L. Marks, B. J. Davis, S. A. Boppart, and P. Carney, "Partially coherent illumination in full-field interferometric synthetic aperture microscopy," *J. Opt. Soc. Am. A* **26**(2), 376–386 (2009).
26. D. L. Marks, T. S. Ralston, S. A. Boppart, and P. S. Carney, "Inverse scattering for frequency-scanned full-field optical coherence tomography," *J. Opt. Soc. Am. A* **24**(4), 1034–1041 (2007).
27. T. S. Ralston, D. L. Marks, P. S. Carney, and S. A. Boppart, "Real-time interferometric synthetic aperture microscopy," *Opt. Express* **16**(4), 2555–2569 (2008).
28. A. Ahmad, N. D. Shemonski, S. G. Adie, H. S. Kim, W. M. Hwu, P. S. Carney, and S. A. Boppart, "Real-time *in vivo* computed optical interferometric tomography," *Nat. Photonics* **7**(6), 444–448 (2013).
29. N. Ji, D. E. Milkie, and E. Betzig, "Adaptive optics via pupil segmentation for high-resolution imaging in biological tissues," *Nat. Methods* **7**(2), 141–147 (2010).
30. W. Lo, Y. Sun, S.-J. Lin, S.-H. Jee, and C.-Y. Dong, "Spherical aberration correction in multiphoton fluorescence imaging using objective correction collar," *J. Biomed. Opt.* **10**(3), 034006 (2005).
31. Y. Jian, R. J. Zawadzki, and M. V. Sarunic, "Adaptive optics optical coherence tomography for *in vivo* mouse retinal imaging," *J. Biomed. Opt.* **18**(5), 056007 (2013).
32. S. G. Adie, B. W. Graf, A. Ahmad, P. S. Carney, and S. A. Boppart, "Computational adaptive optics for broadband optical interferometric tomography of biological tissue," *Proc. Natl. Acad. Sci. U.S.A.* **109**(19), 7175–7180 (2012).
33. S. G. Adie, N. D. Shemonski, B. W. Graf, A. Ahmad, P. Scott Carney, and S. A. Boppart, "Guide-star-based computational adaptive optics for broadband interferometric tomography," *Appl. Phys. Lett.* **101**(22), 221117 (2012).
34. A. Kumar, W. Drexler, and R. A. Leitgeb, "Subaperture correlation based digital adaptive optics for full field optical coherence tomography," *Opt. Express* **21**(9), 10850–10866 (2013).
35. B. W. Graf, S. G. Adie, and S. A. Boppart, "Correction of coherence gate curvature in high numerical aperture optical coherence imaging," *Opt. Lett.* **35**(18), 3120–3122 (2010).
36. J. W. Goodman, *Introduction to Fourier Optics*, 3rd ed. (Roberts and Company Publishers, 2005).
37. S. G. Adie, B. W. Graf, A. Ahmad, B. Dabarsyah, S. A. Boppart, and P. S. Carney, "The impact of aberrations on object reconstruction with interferometric synthetic aperture microscopy," *Proc. SPIE* **7889**, 78891O (2011).
38. S. Gabarda and G. Cristóbal, "Blind image quality assessment through anisotropy," *J. Opt. Soc. Am. A* **24**(12), B42–B51 (2007).

39. V. Lakshminarayanan and A. Fleck, "Zernike polynomials: a guide," *J. Mod. Opt.* **58**(7), 545–561 (2011).
 40. J. R. Fienup and J. J. Miller, "Aberration correction by maximizing generalized sharpness metrics," *J. Opt. Soc. Am. A* **20**(4), 609–620 (2003).
 41. G. Partadiredja, R. Miller, and D. E. Oorschot, "The number, size, and type of axons in rat subcortical white matter on left and right sides: a stereological, ultrastructural study," *J. Neurocytol.* **32**(9), 1165–1179 (2003).
 42. B. W. Graf and S. A. Boppart, "Multimodal *in vivo* skin imaging with integrated optical coherence and multiphoton microscopy," *IEEE J. Sel. Top. Quantum Electron.* **18**(4), 1280–1286 (2012).
 43. R. S. Gurjar, V. Backman, L. T. Perelman, I. Georgakoudi, K. Badizadegan, I. Itzkan, R. R. Dasari, and M. S. Feld, "Imaging human epithelial properties with polarized light-scattering spectroscopy," *Nat. Med.* **7**(11), 1245–1248 (2001).
 44. P. Corcuff, C. Bertrand, and J. L. Leveque, "Morphometry of human epidermis *in vivo* by real-time confocal microscopy," *Arch. Dermatol. Res.* **285**(8), 475–481 (1993).
-

1. Introduction

High-speed and high-resolution volumetric imaging is important for many areas of biology and medicine. For example, real-time imaging with cellular/subcellular-level resolution would improve imaging for intraoperative application and early cancer screening. Confocal microscopy [1], multiphoton microscopy [2], and optical coherence tomography (OCT) [3,4] are powerful techniques to image thick specimens and visualize microstructure in scattering tissue. High-speed confocal and multiphoton microscopy generate depth-sectioned images by scanning a focus across tissue through a high-numerical-aperture objective lens to achieve superior axial and transverse resolution for cellular imaging. To acquire a three-dimensional (3D) image volume, however, these techniques require a depth scan after which the different *en face* images are concatenated to form a so-called z-stack. This method is time consuming, and consequently is susceptible to motion artifacts. On the other hand, OCT utilizes low-coherence interferometry to measure the backscattered light from the sample. Using the so-called coherence gate, the transverse and axial resolutions in OCT are decoupled, and good axial resolution and large depth-of-field in scattering tissues are achieved by using a lower numerical aperture objective lens. As a result, for spectral-domain OCT (SD-OCT), raster scanning the beam in a transverse 2D plane allows 3D, volumetric imaging of the sample. However, the transverse resolution of OCT determined by the numerical aperture (NA) of the objective is usually 10–20 μm , which is insufficient to resolve cellular and subcellular features. Optical coherence microscopy (OCM) can be considered a combination of OCT and confocal microscopy. In addition to cellular level resolution in both the transverse and axial directions [5–7], OCM can achieve better image contrast and greater imaging depth by enhancing the rejection of multiply scattered light over noninterferometric and wide-field methods [8]. A high-NA objective lens is used to focus the optical beam tightly into the tissue and only provides *en face* imaging due to its very short confocal parameter. Therefore, there is a well-recognized tradeoff between the lateral resolution and the depth-of-focus.

To obtain 3D volumetric imaging with high transverse resolution, several methods have been developed for OCM, such as mechanical depth scanning [9–11], voltage-addressable focus shifting [12], and multi-beam focusing [13]. Various focus-depth extension methods have also been proposed and have shown potential for fast high resolution volumetric imaging, including hardware solutions, software additions, or a combination of the two. Examples are Bessel beam illumination [14,15], phase apodization [16], holoscopy [17], depth-encoded synthetic aperture [18], numerical refocusing [19], deconvolution [20], subaperture correlation based digital adaptive optics [21], and interferometric synthetic aperture microscopy (ISAM) [22,23]. Specifically, ISAM is a computed optical imaging technique that can achieve a spatially invariant lateral resolution for all the depths in the acquired 3D data set simultaneously by solving the inverse scattering problem. It is compatible with most common OCT/OCM system setups [24–27] and promising for many biomedical applications. Recently ISAM has been demonstrated as a robust technique for real-time *in vivo* volumetric imaging [28].

As the NA of the objective is increased to obtain better transverse resolution, wavefront aberrations become more evident. The traditional methods for correcting a wide range of optical aberrations require complicated and expensive optical instrumentation. However, even if the imaging system is well-designed, the specimen itself can also introduce aberrations [29]. Two common techniques use objectives with correction collars [30] or integrate adaptive optics [31]. But these methods increase system complexity and in general do not correct depth-dependent aberrations throughout the volumetric data set. In addition, the aberration correction needs to be optimized at the time of imaging, which is a challenge in certain applications. Previously, we have proposed a computed technique, computational adaptive optics (CAO) [32, 33], to correct aberrations in OCT, which uses an existing OCT/OCM system to correct the aberrations of the 3D volume during post-processing. Recently, a sub-aperture correlation-based digital adaptive optics technique has been developed to correct the aberrations. This method can directly provide the local wavefront gradient and automatically correct the aberrations without knowing the system parameters [21,34]. When compared to traditional z-stacking, these computational techniques provide a high-speed volumetric recording rate.

Until recently, ISAM and CAO experiments have been implemented in relatively low NA imaging systems (less than NA = 0.1). The resolution in these systems is not sufficient for cellular/subcellular imaging. In this paper, we constructed a high-resolution spectral-domain OCM (SD-OCM) system and utilized the combination of ISAM and CAO for high-speed volumetric imaging with cellular resolution. *Ex vivo* human breast tissue, *ex vivo* mouse brain tissue, *in vitro* cell dynamics in a 3D scaffold, and *in vivo* human skin were imaged to demonstrate the ability of this technique.

2. Methods

2.1 ISAM and CAO processing

Let $\tilde{S}(x, y, k)$ be the measured SD-OCM signal after wavenumber linearization with (x, y) as the transverse spatial dimensions. The 2D transverse Fourier transform of $\tilde{S}(x, y, k)$ is given by the expression [19]:

$$\tilde{\tilde{S}}(q_x, q_y, k) = H(q_x, q_y, k) \tilde{\tilde{\eta}} \left[q_x, q_y, -\sqrt{(2k)^2 - (q_x^2 + q_y^2)} \right], \quad (1)$$

where $\tilde{\tilde{\eta}}$ is the 3D Fourier transform of the attenuated scattering potential $\eta(x, y, z) = \rho(z) \eta_0(x, y, z)$ and $\eta_0(x, y, z)$ is the scattering potential of the specimen to be detected. When within one Rayleigh length of the optical focus, $\rho(z) = 1$, while beyond one Rayleigh length, the signal decays as $\rho(z) = 1/z$ [24]. In Eq. (1), k is the wavenumber, (q_x, q_y) are the transverse spatial frequencies, and $H(q_x, q_y, k)$ gives the space-invariant axial and transverse spatial frequency response of the (ideal) system. The factor of 2 in Eq. (1) comes from the double-pass (reflection imaging) geometry. To properly invert Eq. (1), regularization (e.g. Tikhonov regularization) must also be performed. However, since $H(q_x, q_y, k)$ is a smooth (within the system passband) Fourier-domain weighting, it represents simple linear shift-invariant filtering that will not introduce major distortions to the image [24,27,28,32]. For fast calculation, we neglect the Fourier-domain reweighting and implement only the resampling:

$$\tilde{\tilde{\eta}}^+ (q_x, q_y, q_z) \approx \tilde{\tilde{S}}(q_x, q_y, k) \Big|_{k=\frac{1}{2}\sqrt{q_z^2 + q_x^2 + q_y^2}} \quad (2)$$

where q_z is the axial spatial frequency. For ISAM processing, resampling ($k \rightarrow q_z$) is performed in the Fourier domain to achieve a spatially invariant transverse resolution. The inverse problem, the inverse Fourier transform is applied and the 3D scattering potential of the specimen can be retrieved:

$$\eta(x, y, z) = \mathbb{F}^{-1} \left[\tilde{\tilde{\eta}}^*(q_x, q_y, q_z) \right] \quad (3)$$

where \mathbb{F}^{-1} stands for the 3D inverse Fourier transform. We note that the resampling in Eq. (2) can be divided into two separate 2D resampling steps to reduce memory requirements for real-time processing on a GPU [28].

If there are aberrations in the optical system, it is equivalent to the fact that the pupil function, which is the scaled Fourier transform of the point spread function (PSF), has a non-uniform phase distribution. We introduce a phase function $H_A(q_x, q_y, k)$ to capture the aberrated transfer function, Eq. (1) can thus be modified as [32]

$$\tilde{\tilde{S}}_A(q_x, q_y, k) = H_A(q_x, q_y, k) H(q_x, q_y, k) \tilde{\tilde{\eta}} \left[q_x, q_y, -\sqrt{(2k)^2 - (q_x^2 + q_y^2)} \right] \quad (4)$$

In hardware adaptive optics, the phase profile of the objective lens pupil is physically modified [32]. In CAO, we numerically modify the phase of a computed pupil function by multiplying the aberration correction filter $H_{AC}(q_x, q_y, k) = H_A^*(q_x, q_y, k)$ (the asterisk ‘*’ represents phase conjugation) with $\tilde{\tilde{S}}_A$ to compensate the aberration, producing

$$\tilde{\tilde{S}}_{AC}(q_x, q_y, k) = H_{AC}(q_x, q_y, k) \tilde{\tilde{S}}_A(q_x, q_y, k) \quad (5)$$

$H_{AC}(q_x, q_y, k)$ can be expressed as a phase function of Zernike polynomials [32] or it can be obtained by the guide star method [33]. After that, an inverse Fourier transform is applied to obtain the aberration-corrected reconstruction.

In practice, an efficient way to correct the 3D aberration is to first apply ISAM processing to correct the 3D defocus and then apply CAO for the *en face* plane images to correct the residual higher order aberrations. Hence, by combining Eqs. (2), (3), and (5), spatially invariant transverse resolution and aberration-free 3D reconstructions of OCM data are achieved in post-processing. In the current CAO method, we take a 2D Fourier transform of the *en face* plane image (complex) to obtain the virtual pupil function and multiply the phase filter H_{AC} to correct the aberration, and then use the inverse Fourier transform to obtain the aberration-corrected reconstruction. For the CAO method using Zernike polynomials, the phase filter H_{AC} is expressed as a phase function of a summation of Zernike polynomials. We manually adjust the coefficients of the Zernike polynomials and use image metrics to assess the image quality. For the point-like structures, or tissue containing a point-like signal, this point-like signal can be chosen as a guide star. The aberration H_A is sensed by the phase difference between the virtual pupil functions of the aberrated guide star signal and the corresponding target PSF. The phase filter H_{AC} can be obtained as the phase conjugation of the aberrated transfer function H_A . A more detailed explanation and implementation could be found in Ref [32] and [33].

2.2 Experimental setup

The experimental system is shown in Fig. 1. Measurements were acquired with a fiber-based spectral-domain (SD) OCM system based on a Michelson interferometer with a 50/50

coupler. Centered at 860 nm, a superluminescent diode (SLD) with a bandwidth of approximately 80 nm was used as the light source, giving a calculated axial resolution of 4.1 μm (Full Width at half Maximum, FWHM) in air. The spectrometer (Bayspec, Inc.) with a 4096 pixel line-scan camera (spL4096-140km, Basler) was interfaced to the PC via a National Instruments IMAQ board (NI-PCIe 1427) and operated at an A-scan rate of 60 kHz. The sample arm was built as a cage system to reduce phase fluctuations. With this high-speed recording rate and rigid system design, phase stability was assured during the imaging process and no phase noise correction was required [22]. A closely-spaced pair of galvanometer scanning mirrors (Cambridge Technology) was utilized for two-dimensional transverse scanning, which provided a compact geometry. The center point between the mirrors was imaged to the pupil plane in the objective lens (LUCPLFLN40X, Olympus, NA = 0.6) through a scan lens ($f = 75$ mm, AC254-075-B, Thorlabs) and a tube lens ($f = 180$ mm, U-TLUIR, Olympus). The coherence gate curvature caused by the non-telecentric setup, where the pivot of the scanning mechanism was not perfectly imaged to the back focal plane of the objective, was corrected computationally [35]. The system was constructed as an inverted microscope and the sample was placed on a coverslip with its surface of interest facing downward, which made it straightforward to obtain a flat optical surface suitable for live-cell studies. The power applied on the sample was about 3 mW, and the sensitivity of the system was 87 dB.

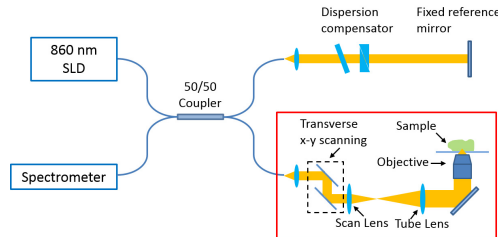


Fig. 1. Schematic of the inverted spectral-domain optical coherence microscope (SD-OCM) system operating with ISAM and CAO.

The transverse resolution, measured by sub-resolution particles (copper zinc iron oxide particles in PDMS, mean diameter < 100 nm), was found to be 0.6 μm (FWHM of the intensity profile). Figure 2 shows an OCM image of a USAF resolution target, where the finest structure (element 3 bars in group 9) can be clearly observed (1.56 μm spacing). The dip-to-peak ratio is approximately 30%, which is sufficient to distinguish the adjacent bars [36]. The high transverse and axial resolution provides the capability for cellular and subcellular level imaging. For an ideal Gaussian beam, the theoretical Rayleigh length is 0.8 μm . The measured Rayleigh length was 3.8 μm , which is larger than the theoretical value due to the aberrations.

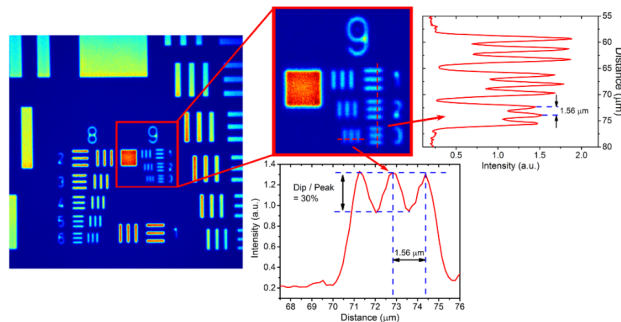


Fig. 2. System characterization. OCM image of a USAF resolution target where the smallest element 3 bars in group 9 can be observed.

3. Experimental results

3.1 Phantom imaging

A tissue mimicking phantom consisting of copper zinc iron oxide particles (< 100 nm) embedded in PDMS was used to quantitatively evaluate the reconstruction quality. Figure 3(a) shows the average PSF FWHM as a function of distance from the focus for OCM, ISAM, and the combination of ISAM and CAO. It can be seen that for this high-NA setup, the transverse resolution degrades (the FWHM of PSF increases) quickly at planes that are away from the focus (green line). ISAM tends to smooth the rapid change in the PSF FWHM and provides a much flatter trend around the focus (red line). We noticed that the presence of aberrations dramatically affects the reconstruction results of ISAM, especially for the far-from-focus region [37]. Using Zernike polynomials and a guide star technique, CAO corrects the aberrations. The blue line shows a PSF width of less than $1 \mu\text{m}$ for all depths after applying both CAO and ISAM.

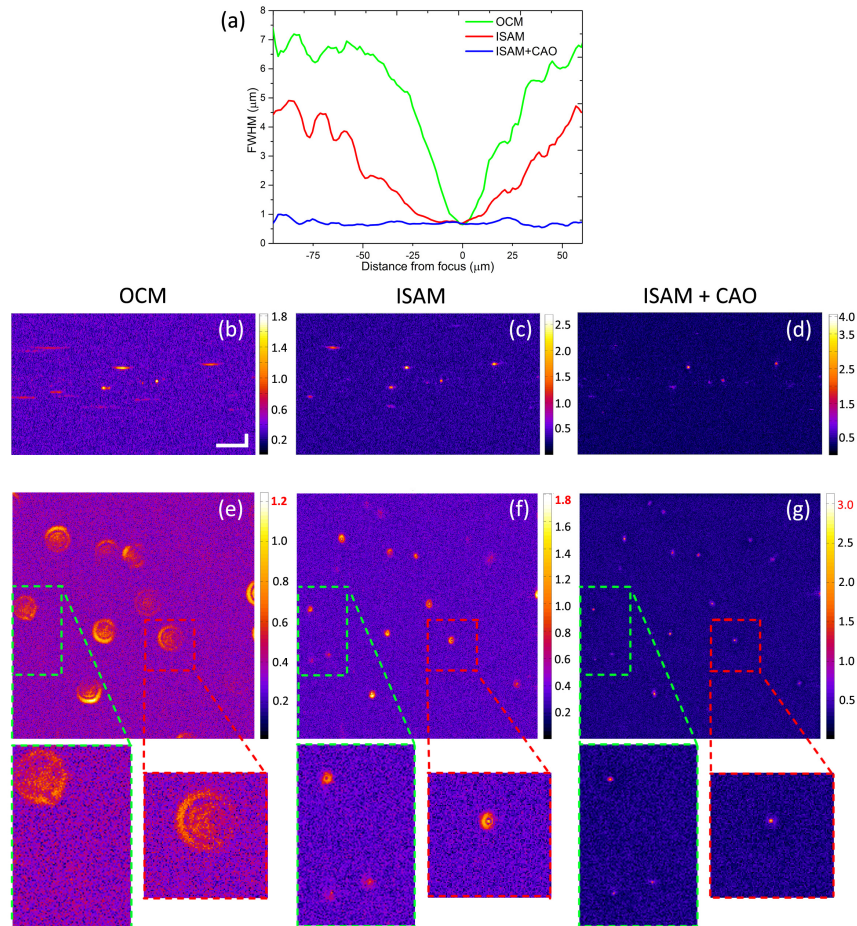


Fig. 3. Tissue phantom imaging (a) Experimental measurement of PSF (FWHM) versus distance from the focus for OCT, ISAM, and the combination of ISAM and CAO. (b)-(d) Cross-sectional images of the reconstructions of OCM, ISAM, the combination of ISAM and CAO. (e)-(g) *En face* plane reconstructions of OCM, ISAM, the combination of ISAM and CAO, at $28 \mu\text{m}$ below the focus. Spherical aberration can be seen clearly in the (e) OCM and (f) ISAM results. The insets show the zoomed-in images of selected particles in (e)-(g). All the images have the same gamma correction. The color scales indicate the displayed range of relative signal amplitudes. The scale bar denotes $20 \mu\text{m}$.

Figures 3(b)-3(d) are cross-sectional images and Figs. 3(e)-3(g) are *en face* imaging results showing the influence of aberrations and the correction ability of CAO. From Figs. 3(b)-3(d), the narrower width of the point scatterers can be clearly seen along the depths. Because we used a phantom with sparse particles and the energy was focused into a much smaller space after the correction, especially in the transverse direction, some blurry patterns in the OCM cross-sectional images disappear in the ISAM and ISAM + CAO results. More detailed improvement can be seen from the *en face* images in Figs. 3(e)-3(g). The *en face* planes are at 28 μm below the focus, extracted from the same 3D data set in Fig. 3(a). The same gamma correction ($\gamma = 0.5$) was applied to the intensity scale of the three images to compress dynamic range. In Fig. 3(e), the ring-shaped structures caused by spherical aberrations can be clearly observed. The rings in the PSF are not circularly symmetric, indicating that other aberrations such as coma or astigmatism are present as well. Although ISAM [Fig. 3(f)] observably reduces the width of the PSF, the ring structures are still present. In Fig. 3(g), the combination of ISAM and CAO shows a significant improvement in the PSF. The sub-resolution particles are imaged as point-like structures, as they would be in the focus of the beam. From the color scale of the color bar, we can see that the highest intensity of the image (red) has been increased to more than 2.5 times (3.0/1.2) that from the combination of ISAM and CAO [Fig. 3(g)], compared to the OCM image alone [Fig. 3(e)].

3.2 *Ex vivo* cellular imaging

Figure 4 shows a series of *en face* images taken at different depths from a 3D reconstructed data set of *ex vivo* human breast tissue. The 1st row (a-c) shows the OCM-processed results while the 2nd row (d-f) shows the ISAM-processed results. Figures 4(a), 4(d) are the *en face* images at the focal plane, which are about 80 μm (optical) below the surface of the sample. Subcellular structures are clearly resolved by both OCM and ISAM. The fat cell membrane boundaries are sharp and the nuclei are readily distinguished as bright and highly scattering (indicated by the arrows).

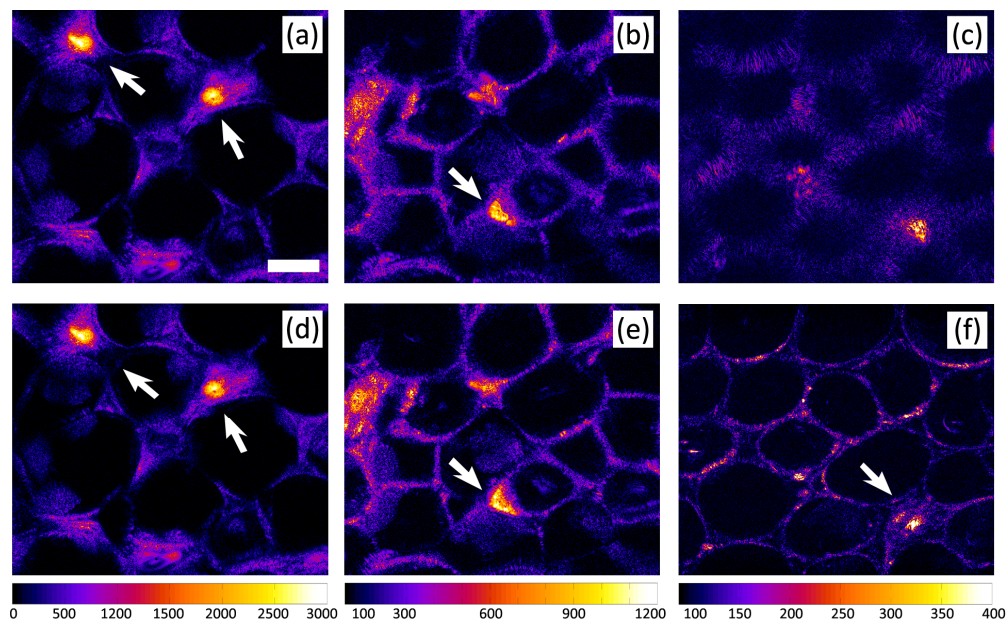


Fig. 4. OCM (1st row) and ISAM (2nd row) in *ex vivo* human breast tissue. *En face* planes of OCM at (a) the focal plane, a plane (b) 22 μm (5.8 Rayleigh lengths) and (c) 67 μm (17.6 Rayleigh lengths) above the focus plane. (d)-(f) ISAM reconstruction of the same *en face* planes of (a)-(c). The bright and highly scattering nuclei are indicated by the arrows. The scale bar in (a) denotes 50 μm , and applies to all images.

However, as we move away from the focal plane the OCM images appear blurry due to the short confocal parameter, as seen in Figs. 4(b), 4(c), which are *en face* planes taken at 22 μm (5.8 Rayleigh lengths) and 67 μm (17.6 Rayleigh lengths) above the focal plane. In comparison, ISAM significantly improves OCM images by keeping the membrane boundaries sharp over different depths, revealing a spatially invariant high transverse resolution. As a result, ISAM dramatically extends the depth-of-field of OCM while maintaining the high transverse resolution. Using ISAM, 3D volumetric cellular imaging can be performed without scanning the focus in depth.

Two image metrics were computed to quantitatively evaluate the image quality along the depth. These plots are shown in Fig. 5. The first plots the depth-dependent signal-to-noise ratio (SNR) improvement. We used 90% quantiles of the intensity histograms as the depth-dependent signal [28] and the minimum local standard deviation of the image as the noise, which indicated the fluctuation of the background. The subtraction between the SNR of the ISAM data and the SNR of the OCM data shows the SNR improvement. The other image metric utilized was anisotropy, which measured the variance of the entropy upon a set of directions. This metric was originally devised to identify in-focus, noise-free images from other degraded versions in incoherent imaging systems [38]. Higher values in this metric indicate sharper structures and better image quality. From Fig. 5 we can see that these two image metrics show good agreement, and ISAM processing gives better image quality than OCM along different depths. Better SNR improvement is observable at the planes further from the focus because of the defocus correction. As the fat cells may act as a ball lens array, stronger signal was observed at the top and bottom membrane surfaces, which generated two main peaks (depth = 0 and depth at the focal plane) in Fig. 5(b).

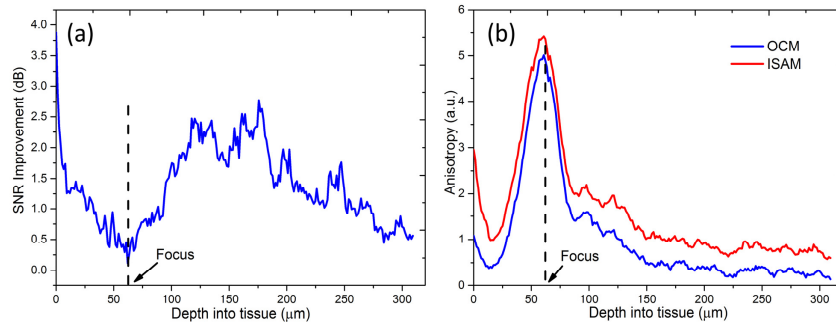


Fig. 5. Image metrics for quantitatively evaluating the image quality of *ex vivo* human breast tissue along the depth. (a) Depth-dependent SNR improvement, based on subtracting the SNR between ISAM and OCM. (b) Image anisotropy measurement.

As a high-NA objective was used in the experiment, images are more sensitive to aberration, which may be caused by elements or misalignments within the optical imaging system or by the sample itself [29]. CAO provides a new way to correct the aberrations after acquiring the data. To demonstrate the further image improvement of utilizing CAO, Fig. 6 shows *en face* planes (about 6 Rayleigh lengths above the focus) from tomograms of an *ex vivo* mouse brain tissue (coronal section). From the ISAM-processed results [Fig. 6(b)], it can be seen that not only the cell bodies of neurons (dark regions, indicated by the blue arrows), but also the myelinated axons (the bright lines, indicated by the green arrows) are clearer compared to the OCM results [Fig. 6(a)]. To correct these aberrations, we applied CAO with Zernike polynomials [39] $Z_{3,5}$ (astigmatism), Z_4 (defocus), $Z_{7,8}$ (coma), Z_{12} (spherical aberration) to modify the virtual pupil function of the *en face* plane and used image metrics (anisotropy [38] and power of image intensity [40]) for adjustment feedback. After CAO processing, Fig. 6(c) shows sharper features of the axons. The insets in Figs. 6(b), 6(c) show average profiles of myelinated axons and their quantified diameters by FWHM. The

measured results of the myelinated axons (1.00 μm and 1.23 μm), after aberration correction, more closely match the known anatomical size range (0.1-1.5 μm) [41]. This verifies that the combination of ISAM and CAO can further improve the resolution and image quality for volumetric cellular imaging.

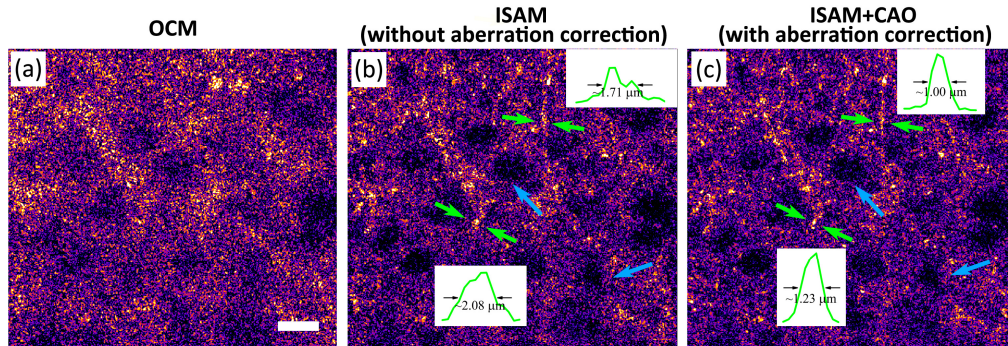


Fig. 6. *En face* planes from highly scattering *ex vivo* mouse brain tissue at a depth ~ 6 Rayleigh lengths above the focus, showing (a) OCM, (b) Uncorrected ISAM, and (c) CAO aberration-corrected ISAM. The blue arrows indicate the cell bodies of neurons, and the green arrows indicate the myelinated axons. The insets show the profile and FWHM of the myelinated axons. The scale bar denotes 20 μm .

3.3 *In vitro* cell dynamics

Because ISAM can dramatically extend the depth-of-field of normal OCM with high transverse resolution, it can achieve 3D volumetric cellular imaging by high-speed 2D scanning, which is promising for research investigating fast cell dynamics. Cell activities in 3D topographic scaffold structures are of great interest in tissue engineering research. In this paper, we use ISAM and CAO to investigate the dynamics of mouse dermal fibroblast cells in 3D macroporous alginate hydrogel scaffolds.

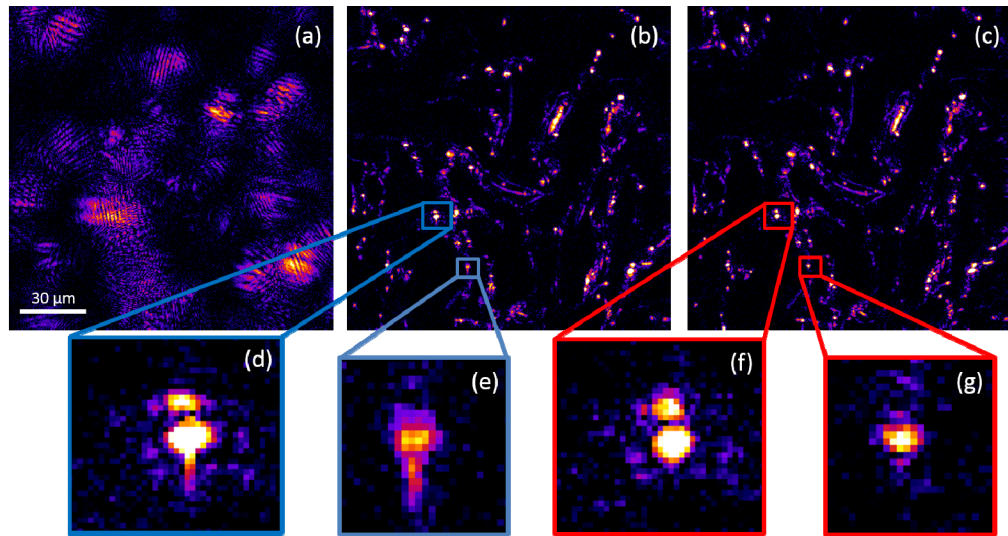


Fig. 7. *En face* plane reconstructions of the 3D scaffold at a depth of about 11.5 Rayleigh lengths above the focus from (a) OCM, (b) ISAM without aberration correction, and (c) CAO and ISAM. The images in (f) and (g) show the same zoomed-in structures as in (d) and (e), but show the results of correcting the aberrations. The scale bar denotes 30 μm .

The 3D volumes were acquired by 512×512 transverse scanning at an A-scan rate of 60 kHz. Figure 7 shows the reconstruction results of an *en face* plane at about 43.7 μm (~ 11.5

Rayleigh lengths) above the focus. The OCM image [Fig. 7(a)] is quite blurry and it is difficult to recognize the structure of the scaffold. Compared to the OCM result, ISAM dramatically improves the reconstruction and clearly reconstructs the scaffold structures [Fig. 7(b)]. However, astigmatism was noticed as stretched point-like structures. Two representative aberrated structures selected from Fig. 7(b) were examined at high magnification and shown in Figs. 7(d), 7(e). We applied CAO in post-processing to correct these aberrations, as was done for the *ex vivo* brain tissue. The final aberration correction results are shown in Figs. 7(c), 7(f), 7(g). It can be seen that after CAO processing, the tail of the point-like structure has disappeared and better imaging performance is achieved.

Utilizing ISAM and CAO, the size of the 3D volume was about $160\ \mu\text{m} \times 160\ \mu\text{m} \times 70\ \mu\text{m}$, with a lateral resolution of $0.6\ \mu\text{m}$ and an axial resolution of $4\ \mu\text{m}$. The total depth is related to the focus position [28]. Acquisition time of each 3D data set was within 4.4 s and the total time-lapse measurement duration was about 2 hours. Figure 8 shows the results from two time points: 0 min and 112 min. Figures 8(a), 8(d), 8(g), 8(j) and Figs. 8(b), 8(e), 8(h), 8(k) are at the depth of approximately 12 and 5 Rayleigh lengths above the focus, respectively. Compared with traditional OCM, we can see that the scaffold structures at different depths in the 3D volume are clearly resolved by the ISAM/CAO reconstruction. Thus the application of computed imaging to OCM makes it possible to image the interactions between the cells and the scaffold and observe cell migrations over longer distances without having to repeatedly scan the focal plane each time. In this sample, the fibroblast cells mainly moved around within the focal plane [Figs. 8(c), 8(f), 8(i), 8(l)]. Over the course of 2 hours, we can see cells migrating towards the upper right corner. The filopodia were clearly observed during the movement, and are indicated by the arrow in Figs. 8(f), 8(l). The cell migration over 2 hours can be seen in the supplemental [Media 1](#).

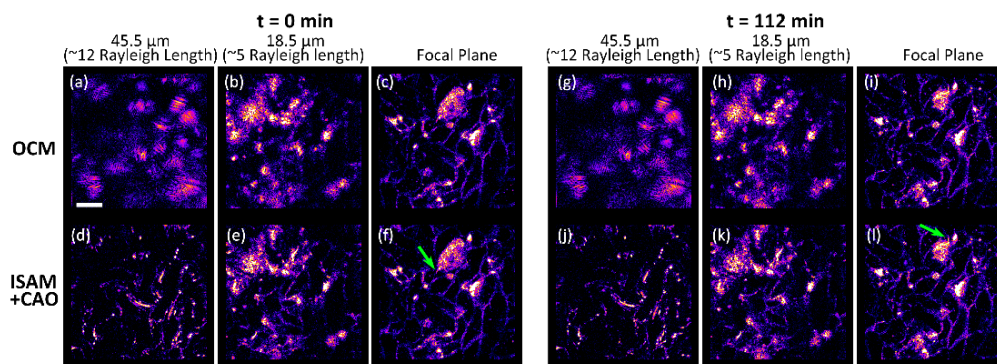


Fig. 8. Time lapse results of mouse dermal fibroblasts in a 3D macroporous alginate hydrogel scaffold ([Media 1](#)). Images (a-f) and (g-l) are the results for $t = 0\ \text{min}$ (start) and $112\ \text{min}$, respectively. The columns (a, d, g, j) are at the depth of about 12 Rayleigh lengths above the focus, and (b, e, h, k) are at the depth of about 5 Rayleigh lengths above the focus. Images (c, f, i, l) are at the focal plane. The top row images (a, b, c, g, h, i) are the OCM results while the bottom row images (d, e, f, j, k, l) show the results from applying the combination of ISAM and CAO. The green arrows indicate the filopodia. The scale bar denotes $30\ \mu\text{m}$.

3.4 *In vivo* cellular imaging

To demonstrate the capability of ISAM and CAO for high-speed, *in vivo* volumetric cellular imaging, 3D data of normal human skin (from the palm) were acquired from a healthy volunteer. An imaging mount, consisting of a coverslip and a rigid holder with a hole in the center, was attached to the cage system and used to keep the skin stabilized during image acquisition, similar in principle to those used for confocal microscopy [1]. Glycerol was applied between the skin and the coverslip to serve as an index-matching agent. All imaging was performed in accordance with a protocol approved by the Institutional Review Board at

the University of Illinois at Urbana-Champaign. The acquired 3D volume with 0.6 μm lateral resolution and 4.1 μm axial resolution was 160 μm \times 160 μm \times 150 μm for x, y, and z dimensions after ISAM and CAO post-processing. The recorded 3D data set consisted of 4,096 pixels per A-scan and 512 A-scans along each transverse dimension. As only 2D transverse scanning was needed our total acquisition time was within 4.4 s, which is significantly faster than previous volumetric OCM acquisition methods that require scanning along the depth to obtain 3D data [42].

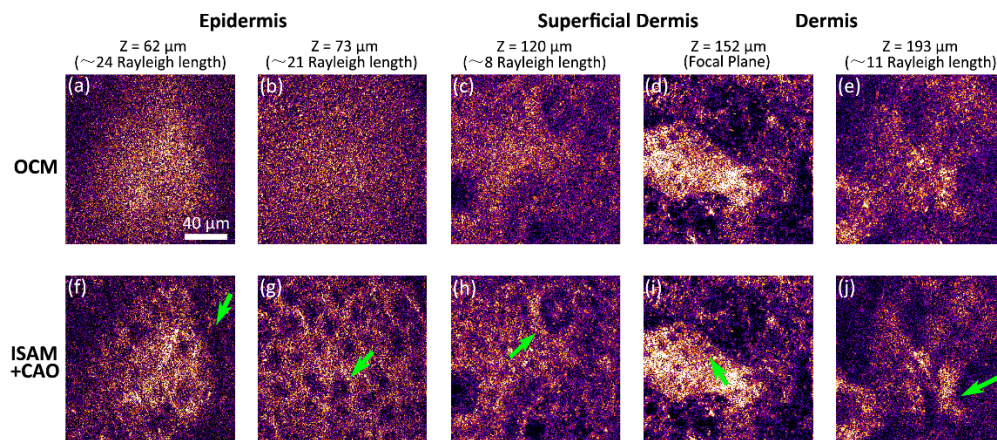


Fig. 9. Cellular resolution images of different layers in *in vivo* human skin. The 1st row are OCM results without Z-stacks, and the 2nd row are the results from the combination of ISAM and CAO. (a, f) Depth about 62 μm beneath the surface and 24 Rayleigh lengths above the focus, where the junction between the stratum corneum and the epidermis is located. The boundary of this junction is indicated by the arrow in (f). (b, g) Epidermis layer. The nuclei of granular cells are visible in ISAM/CAO results (arrow) while they are not present in the OCM result. (c, h) Superficial dermis layer. An arrow shows the dermal papillae. (d, i) Junction between epidermis and dermis. The basal cells are visualized and indicated by an arrow. (e, j) Deep in the dermis, which is about 11 Rayleigh lengths below the focus. Probable collagen fiber bundles are indicated by the arrow in the ISAM/CAO reconstruction. The scale bar in (a) denotes 40 μm , and applies to all images.

Figure 9 shows different *en face* planes extracted from the volumetric data set of the skin. The five columns represent 5 depth reconstructions using OCM and the combination of ISAM and CAO. The focus was placed at an approximate depth of 152 μm beneath the surface, near the junction region between the epidermis and dermis, as shown in Figs. 9(d), 9(i). For the OCM results, only the microstructures located around the focus can be seen. For example, the structures in the *en face* planes at about 24 and 21 Rayleigh lengths above the focus are totally washed out due to the defocus [Figs. 9(a), 9(b)]. As a comparison, after ISAM and CAO processing, the structures within various layers of the skin, from the epidermis through the superficial dermis and into the dermis, are clearly resolved [Figs. 9(f)-9(j)]. At a depth about 62 μm under the skin surface and 24 Rayleigh lengths above the focal plane, the transition between the stratum corneum and the epidermis, the boundary shown by the arrow, can be seen in Fig. 9(f). In Fig. 9(g), the nuclei of the granular cells become visible as dark areas surrounded by bright cytoplasm. Deeper in the skin, dermal papillae are visualized and indicated by the arrow in Fig. 9(h). From Fig. 9(i), we can clearly see the dermal-epidermal junction and the basal cells (indicated by the arrow), which have sizes smaller than the granular cells. Deep into the dermis, heterogeneous structure, most likely representing collagen fiber bundles, can be seen in Fig. 9(j). Overall, ISAM and CAO provide an approach to rapidly image the different layers and structures of *in vivo* human skin with cellular level resolution. It is reported that 85% of skin cancer originates in the epithelial layer [43]. One of the critical steps in differentiating cancer cells is significant nuclear enlargement, where the

nuclei in the basal cell layer has a mean size around 6 μm [44]. Therefore, high resolution imaging of the entire epidermis could provide valuable information for performing skin cancer diagnosis. *In vivo* imaging utilizing ISAM and CAO shows great potential for applications in skin cancer research.

4. Discussion and conclusions

With this high-speed inverted SD-OCM system, we have performed volumetric cellular/subcellular imaging of *ex vivo* human breast tissue, *ex vivo* mouse brain tissue, *in vitro* fibroblast cell dynamics, and *in vivo* human skin tissue. Dramatic improvement of image quality within the entire imaging volume has been achieved by utilizing the computational optical imaging approaches of ISAM and CAO.

It is noted that in CAO, Z_4 of the Zernike polynomials can also be used to correct the defocus on a two-dimensional *en face* plane image. However, it should be pointed out that the phase distribution of Z_4 , $2q_x^2 + 2q_y^2 - 1$, can be recognized as the paraxial approximation of the transfer function in ISAM, $-\sqrt{(2k)^2 - (q_x^2 + q_y^2)}$ in Eq. (1) and Eq. (4). When using a high-NA objective in the experiment (e.g. OCM), the paraxial approximation cannot always be satisfied. A recent publication, Ref [21], also discusses this problem. The fast FM model they used is similar to Z_4 we used in CAO, and the IS method they used is similar to our ISAM technique. Furthermore, ISAM could refocus the out-of-focus points in three dimensions because it solves the 3D inverse scattering problem for aberration-free OCT/OCM, not only dealing with the transverse spatial frequency but also the axial spatial frequency. A more detailed explanation of the transverse and axial blurring resulting from a point scatterer when imaging with high-NA can be found in our previous paper, for example, Fig. 4 and Fig. 5 in Ref [24]. Hence, in practice, an efficient way to correct the 3D aberration is to first apply ISAM processing to correct the 3D defocus and then apply CAO for *en face* plane images to correct the residual higher order aberrations.

In the current CAO using the Zernike polynomials method, manual adjustments to the coefficients was necessary, and an automated approach is currently under development. Although we have achieved a high acquisition rate for 3D cellular imaging by combing ISAM and CAO techniques, a faster processing rate is also very important, especially for medical diagnostics. Our group has succeeded in real-time ISAM and CAO using a guide star method by utilizing a graphics processing unit (GPU). Future work includes developing real-time CAO with automatically processing technique for various types of tissues. A recent publication, Ref. 34, using a sub-aperture correlation method to directly sense the aberration without knowing the parameters of system, is a good inspiration.

Acknowledgments

The authors thank Carle Foundation Hospital for providing access to the human tissue specimens used in this research. This research involving *ex vivo* human breast tissue and *in vivo* imaging in human subjects was conducted under Institutional Review Board protocols approved by the University of Illinois at Urbana-Champaign and Carle Foundation Hospital. We thank Eric Chaney for his assistance with managing these IRB protocols, Kush Paul and Ziad Mahmassani for providing the cell samples, and Darold Spillman for administrative and information technology support related to this research. We also thank the Imaging Technology Group in the Beckman Institute for Advanced Science and Technology for access to the computers used to process the data. This research was supported in part by grants from the National Institutes of Health (1 R01 EB012479, 1 R01 EB013723, and 1 R01 CA166309, S.A.B.). Additional information can be found at <http://biophotonics.illinois.edu>.